Available online at https://link.springer.com/journal/42241
http://www.jhydrodynamics.com
Journal of Hydrodynamics, 2023
https://doi.org/10.1007/s42241-024-0077-8

Numerical analysis of turbulent fluctuations around an axisymmetric body of revolution based on wall-modeled large eddy simulations

Kang-jian He[1], Fu-chang Zhou[2], Wei-wen Zhao[1], Jian-hua Wang[1], De-cheng Wan[1*]
1. *Computational Marine Hydrodynamics Lab (CMHL), School of Naval Architecture, Ocean and Civil Engineering, Shanghai Jiao Tong University, Shanghai 200240, China*
2. *Wuhan Second Ship Design and Research Institute, Wuhan 430205, China*

(Received December 7, 2023, Revised December 26, 2023, Accepted December 29, 2023, Published online January 11, 2024)
©China Ship Scientific Research Center 2024

Abstract: Wall-modeled large eddy simulation (WMLES) is used to investigate turbulent fluctuations around an axisymmetric body of revolution. This study focuses on evaluating the ability of WMLES to predict the fluctuating flow over the axisymmetric hull and analyzing the evolution of turbulent fluctuations around the body. The geometry is the DARPA SUBOFF bare model and the Reynolds number is 1.2×10^7, based on the free-stream velocity and the length of the body. Near-wall flow structures and complex turbulent fluctuation fields are successfully captured. Time-averaged flow quantities, such as time-averaged pressure and skin-friction coefficients, and time-averaged velocity profiles on the stern, achieved great agreements between WMLES results and experimental data. Self-similarity of time-averaged velocity defects within a self-similar coordinate up to twelve diameters from the tail. A comprehensive analysis of second-order statistics in the mid-body, stern, and wake regions is condutced. Numerical results agree well with experimental data and previous wall-resolved large eddy simulation (WRLES) results about root mean square (rms) of radial and axial fluctuating velocities at the stern. Turbulent fluctuations including turbulent kinetic energy (TKE) and second-order velocity statistics are identified as dual peak behavior and non-self-similar over the wake length, consistent with previous findings in the literature. This assessment enhances the understanding of WMLES capabilities in capturing complex fluctuating flow around axisymmetric geometries.

Key words: Turbulent fluctuations, wall-modeled large eddy simulation (WMLES), turbulent boundary layer, wake

0. Introduction

Turbulent fluctuations around underwater vehicles are currently under active study due to its direct relevance to structural vibrations and flow noise. It is a significant flow characteristic which is not only complex for scientific studies, but also important for engineering applications.

The DARPA SUBOFF model is a canonical streamlined body of revolution, which has been widely used as the benchmark model in studies focusing on exploring fluid dynamics phenomena relevant to underwater vehicles. A series of experiments have been conducted[1-3] to study complex turbulent flow around the DARPA SUBOFF model with and without appendages and abundant valuable experimental results about turbulent fluctuations were available.

Numerous relevant numerical studies have also been conducted. Due to the consideration of computational cost, Reynolds averaged Navier-Stokes (RANS) method with turbulence closure models is usually used to solve the time-averaged fields in the early works[4-8]. However, due to the fundamental nature of the averaging process, it is a challenge to RANS to predict unsteady fluctuations in turbulent flow[9-10]. Simulating complex engineering-relevant flows through large eddy simulation (LES) has become increasingly popular in recent years, thanks to advancements in computational capabilities and the optimization of numerical algorithm[11]. Posa and Balaras[12] carried out wall-resolved large eddy simulation (WRLES) about the near-wall flow and wake of DARPA SUBOFF body with appendages. The Reynolds number $Re_L=(U_\infty L)/\nu$ is 1.2×10^6, based on the free-stream velocity u_∞, molecular kinematic viscosity ν, and the length of the body L. The

Project supported by the National Natural Science Foundation of China (Grant No. 52131102).
Biography: Kang-jian He (1999-), Male, Ph. D.,
E-mail: hekangjian@sjtu.edu.cn
Corresponding author: De-cheng Wan,
E-mail: dcwan@sjtu.edu.cn

complexity of the stern flow is analyzed and the source of the bimodal behavior of the turbulent stresses in the wake is traced back to the thick boundary layer over the stern. Kumar and Mahesh[11] presented a numerical analysis of near-wall flow structures and the wake evolution on the bare hull DARPA SUBOFF model at $Re_L = 1.1\times10^6$ using WRLES. To investigate the effect of Reynolds numbers on the flow structure over the stern. Posa and Balaras[13] extended WRLES to resolve the turbulent flows near the stern of flows around DARPA SUBOFF with appendages at $Re_L = 1.2\times10^6$, 1.2×10^7. Their investigation demonstrated that the development turbulent boundary layer (TBL) over the stern was notably affected by the adverse pressure gradient, almost regardless of the Reynolds number. Morse and Mahesh[14] conducted the WRLES to simulate the flow around the DARPA SUBOFF bare model at $Re_L = 1.2\times10^6$ with 7.12×10^8 cells. They introduced a novel approach to analysis the TBL on streamlined bodies in a streamline coordinate system. Their findings reveal that the streamwise curvature has the effect of generating additional pressure gradients normal to the streamlines, leading to significant pressure variations across the boundary layer. Liu et al.[15] applied WRLES method to simulate the flow around the DARPA SUBOFF bare model at $Re_L = 1.2\times10^6$ using 1.476×10^9 meshes. A great agreement with experimental data and previous WRLES results[11] was achieved about the root mean square (rms) of radial and axial velocity on the stern.

It can be seen that WRLES tends to be computationally expensive at high Reynolds numbers. This is due to the need of directly resolving the inner layer of the TBL, where the turbulent scale is identified by the viscous scale $\delta_\nu = \nu / u_\tau$, where u_τ is the friction velocity[16]. Choi and Moin[17] examined the computational cost and showed that the number of grid nodes required WRLES are proportional to $Re_L^{13/7}$. That motivates the idea of modeling flow within the inner layer, while exclusively resolving the outer layer of TBL and the regions beyond the boundary layer. This approach is commonly known as wall-modeled large eddy simulation (WMLES)[18-20], where the required mesh number scales linearly with Re_L. Therefore, this method significantly expanded the range of Reynolds numbers that LES can effectively handle. Zhou et al.[21] employed WRLES and WMLES to investigate an axisymmetric body of revolution. The study specifically targeted a comprehensive analysis of the space-time features of velocity and pressure fluctuations within the boundary layer of the tail cone. The velocity statistics showed robust agreement with experimental results, indicating that the development of TBL in the tail cone was not markedly affected by near-wall structures upstream. Zhou et al.[22] simulated the turbulent flows and noise around the fully appended SUBOFF at $Re_L = 1.2\times10^7$ with WMLES. The noise was calculated by using the Ffowcs Williams and Hawking formulation. Power spectral density of wall fluctuation pressures and directivity feature of radiated noise were obtained and analyzed. Chen et al.[23] investigated the flow around the DARPA SUBOFF bare model at $Re_L = 1.2\times10^7$ using WMLES and focused on time-averaged quantities such as time-averaged pressure and skin-friction coefficients and velocity profiles. The impact of both the wall stress model and sampling distance was also conducted. The recommended wall stress model and sampling distance was given. It should be noted that the ability of WMLES to predict the turbulent fluctuations is not investigated in their research.

In this study, the flow around an axisymmetric body of revolution (DARPA SUBOFF bare model) at $Re_L = 1.2\times10^7$ is numerically investigated using the WMLES. The strategy we followed is guided by the simulation reported by Chen et al.[23] while the main focus is on turbulent fluctuations around the DARPA SUBOFF. The objective of this paper is to evaluate the ability of WMLES to predict turbulent fluctuations over the axisymmetric hull and to investigate the evolution of fluctuation quantities of the flow around the body of the DARPA SUBOFF.

1. Computational method

1.1 *Governing equations*

The study in this paper is conducted with the open-source computational fluid dynamics (CFD) platform OpenFOAM and open-source library, libWallModelledLES, produced by Mukha et al.[24] In WMLES, the unsteady filtered Navier-Stokes equations for incompressible flows are solved:

$$\frac{\partial \tilde{u}_i}{\partial x_i} = 0 \tag{1}$$

$$\frac{\partial \tilde{u}_i}{\partial t} + \frac{\partial \tilde{u}_i \tilde{u}_j}{\partial x_j} = -\frac{1}{\rho}\frac{\partial \tilde{p}}{\partial x_i} + \nu \frac{\partial^2 \tilde{u}_i}{\partial x_j \partial x_j} + \frac{\partial \tau_{ij}^{\mathrm{SGS}}}{\partial x_j} \tag{2}$$

where $\tilde{u}$ and $\tilde{p}$ are filtered velocity and pressure, ρ is the fluid density, ν is the molecular kinematic viscosity of the fluid. The space and time coordinates are denoted by x and t. τ_{ij}^{SGS} is the subgrid-scale

(SGS) stress tensor.

1.2 *The SGS model*

The effect of the scales smaller than the filtered size is modeled by the SGS stress tensor $\tau_{ij}^{\mathrm{SGS}} = 2\nu_{\mathrm{SGS}}\tilde{S}_{ij} + (1/3)\tau_{kk}^{\mathrm{SGS}}\delta_{ij}$, where ν_{SGS} is the SGS eddy viscosity computed by the SGS model. In this paper, the wall-adapting local eddy-viscosity (WALE) SGS model proposed by Nicoud and Ducros[25] is used to model the SGS eddy viscosity. This SGS model is an eddy viscosity model that preserves the simplicity and computational efficiency characteristic of traditional algebraic SGS models. Wall damping effects are considered without the explicit use of damping functions[10]. It is found that this model can predict accurate asymptotic behaviors near the wall, and the eddy viscosity becomes negligible in laminar regions[12]. The SGS eddy viscosity in this model is calculated as

$$\nu_{\mathrm{SGS}} = (C_w\Delta)^2 \frac{(S_{ij}^d S_{ij}^d)^{3/2}}{(\tilde{S}_{ij}\tilde{S}_{ij})^{5/2} + (S_{ij}^d S_{ij}^d)^{5/4}} \tag{3}$$

where C_w is the model constant and is set to 0.325 in this paper, Δ is the grid filter length scale and calculated as the cube root of local cell volume, $\tilde{S}_{ij}$ is the resolved strain-rate tensor and S_{ij}^d is the traceless symmetric part of the square of the velocity gradient tensor.

1.3 *The wall-stress model*

In WMLES, the flow in inner layer region of boundary layer is modeled with the wall-stress model, while flows in the outer layer region and outside the boundary layer are directly resolved. The wall-stress model approximates the RANS equations using a thin-layer approach and incorporates a mixing-length model for the eddy viscosity[26]. The wall-stress model is derived based on the thin boundary layer equations (TBLE)

$$\frac{\partial}{\partial x_2}\left[(\nu+\nu_t)\frac{\partial \overline{u}_i}{\partial x_2}\right] = \frac{1}{\rho}\frac{\partial \overline{p}}{\partial x_i} + \frac{\partial \overline{u}_i}{\partial t} + \frac{\partial \overline{u}_i\overline{u}_j}{\partial x_j} \tag{4}$$

where $i = 1,3$, i.e., wall-parallel directions. whereas the wall-normal velocity u_2 is derived by the continuity equation. ν_t is the eddy viscosity. Terms in the right of Eq. (4) are pressure gradient term, transient term and convective term. In this study, the temporal term and convective term are neglected and the pressure gradient term is only explicitly taken into account, which is called the non-equilibrium wall-stress model (NEQWM)**.** Then the TBLE is simplified to ordinary differential equations and beneficial for solving. NEQWM has obtained widespread attention due to the role of the adverse pressure gradient in the process of flow separation. In Chen et al.[23], it has been shown NEQWM can give great results for the flow under the adverse pressure gradient around the DARPA SUBOFF. Therefore, NEQWM is adopted in this study.

In the wall-stress model, pertinent components related to velocity and pressure are sampled from the cell center, specifically at a user-defined sampling distance h from the wall. Subsequently, the wall shear stress is computed using the wall stress model and applied at the corresponding center of the boundary face. More details about the process of wall-stress model can refer to Mukha et al.[24] In this study, the sampling distance h is defined as the distance between the center of the third wall-normal cell and the wall, as recommended by Chen et al.[23].

2. Computational set-up

2.1 *Geometry and computational domain*

The DARPA SUBOFF hull without appendages is adopted as the computational model in this study. Figure 1 shows the axisymmetric bare hull configuration of the DARPA SUBOFF. This model is an axisymmetric body of revolution with both lateral and longitudinal curvatures and widely used for researches. The maximum diameter is $D = 0.508\,\mathrm{m}$ and the whole length is $L = 8.6D$. The Reynolds number Re_L is 1.2×10^7 consistent with the experiment[1].

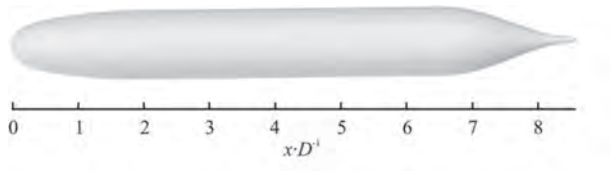

Fig. 1 The DARPA SUBOFF hull without appendages

A schematic of the computational domain is shown in Fig. 2. The computational domain is set following the work of Chen et al.[23]. The origin of the reference coordinate system is set at the nose of the model. The x axis is parallel with the streamwise direction and the direction of z axis is vertically upward. The inlet is located $1.0D$ in front of the nose of the model, and the outlet is located $3.0D$ downstream of the stern. The lateral sides are located $1.0D$ from the bow of the model to reduce the boundary effect.

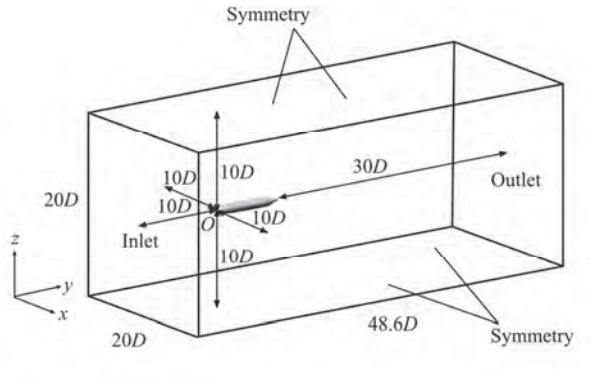

Fig. 2 The computational domain

The boundary condition of inlet is set as uniform inflow $(u_\infty, 0, 0)$, where u_∞ is the free-stream velocity. For the outlet, the Neumann boundary condition of zeroGradient in OpenFOAM is applied. The symmetry boundary condition is used elsewhere.

2.2 *Mesh arrangement*

Unstructured meshes are used and generated by snappyHexMesh utility. The layout of mesh is set according to Chen et al.[23]. However, the size of mesh in wall-parallel directions is refined to capture more detail information about fluctuating flow around the DARPA SUBOFF. As a result, the boundary layer mesh in wall-parallel directions has a uniform size of $\Delta x = \Delta z = (1/25)\delta$ and the height of the wall-adjacent layer is $\Delta y_w = (1/50)\delta$, δ is the boundary layer thickness, which is firstly estimated with the empirical formula for a flat plate and corrected with the solution of the steady RANS simulation. The expansion ratio of mesh is set as 1.03. More details about the generation and layout of computational meshes can refer to Chen et al.[23]. The computational mesh near the hull is shown in Fig. 3 and the final total number of mesh is about 8.4×10^7.

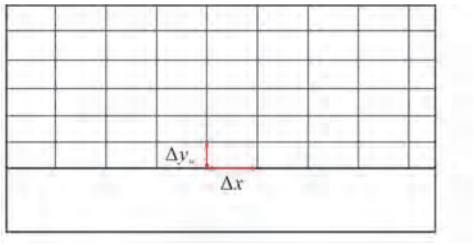

Fig. 3 (Color online) The computational mesh near the hull

2.3 *Numerical schemes*

The numerical simulation is firstly conducted with the steady RANS simulation with k-ω SST turbulence model[27] and converged solutions including pressure and velocity are obtained. Then the pressure and velocity are used as the initial condition of WMLES. Numerical schemes about the temporal discretization and spatial discretization for RANS and WMLES are set following Chen et al.[23].

2.4 *Time step and solution time*

The simulation is performed with a non-dimensional time step of $u_\infty \Delta t / L = 3\times10^{-5}$. The solution time is equal to 5.35 flow-through times. The maximum Courant Friedrichs-Lewy number is less than 0.3. The flow quantities are collected for the last two flow-through times for statistics analysis.

3. Results and discussions

3.1 *Overview of the flow field*

Instantaneous near-wall flow structures around the hull shown in Fig. 4 are identified using the modified normalized Liutex-Omega method[28-29] and colored by axial velocity nondimensionalized by the income flow velocity u_∞. $\tilde{\Omega}_R$ is a scalar and defined as

$$\tilde{\Omega}_R = \frac{\beta^2}{\beta^2 + \alpha^2 + \lambda_{cr}^2 + 0.5\lambda_r^2 + \varepsilon} \tag{5}$$

where $\alpha = 0.5\sqrt{(\boldsymbol{\omega}\cdot\mathbf{r})^2 - 4\lambda_{ci}^2}$, $\beta = 0.5\boldsymbol{\omega}\cdot\mathbf{r}$, $\boldsymbol{\omega}$ is the vorticity vector, $\mathbf{r}$ is the normalized real eigenvector of the velocity gradient tensor, λ_{cr} and λ_r are real part of conjugate complex eigenvalues and real eigenvalues of velocity gradient tensor, λ_{ci} is the imaginary part of the complex eigenvalue. $\varepsilon = b_0(\beta^2 - \alpha^2)_{\max}$, b_0 is recommended to be 10^{-6} in marine hydrodynamics. The threshold value of isosurface of $\tilde{\Omega}_R$ is set as the recommended value 0.52[30].

Figure 5 provides a global view of the instantaneous normalized axial velocity, pressure coefficient, and vorticity magnitude field on the xoz plane. The black solid lines represent the surface of hull. These figures are plotted with Turbulucid[31], which is a package for post-processing two-dimensional cell-centered VTK polyData. The pressure coefficient is defined as

$$C_p = \frac{p - p_\infty}{0.5\rho u_\infty^2} \tag{6}$$

where p_∞ is the reference pressure.

The flow firstly experiences acceleration at the

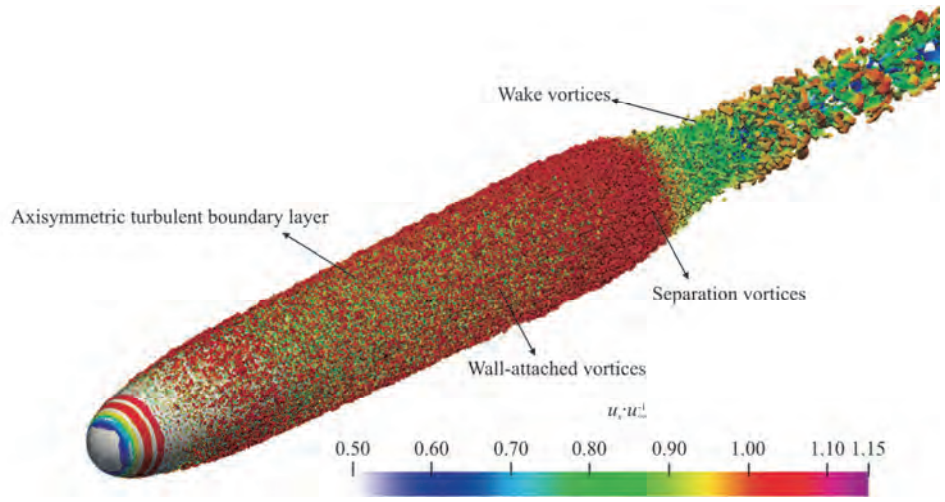

Fig. 4 (Color online) Instantaneous near-wall flow structures around the hull are visualized using the modified normalized Liutex-Omega method[28-29] $(\bar{\Omega}_R = 0.52)$. The isosurface is colored by axial velocity nondimensionalized by the income flow velocity u_∞

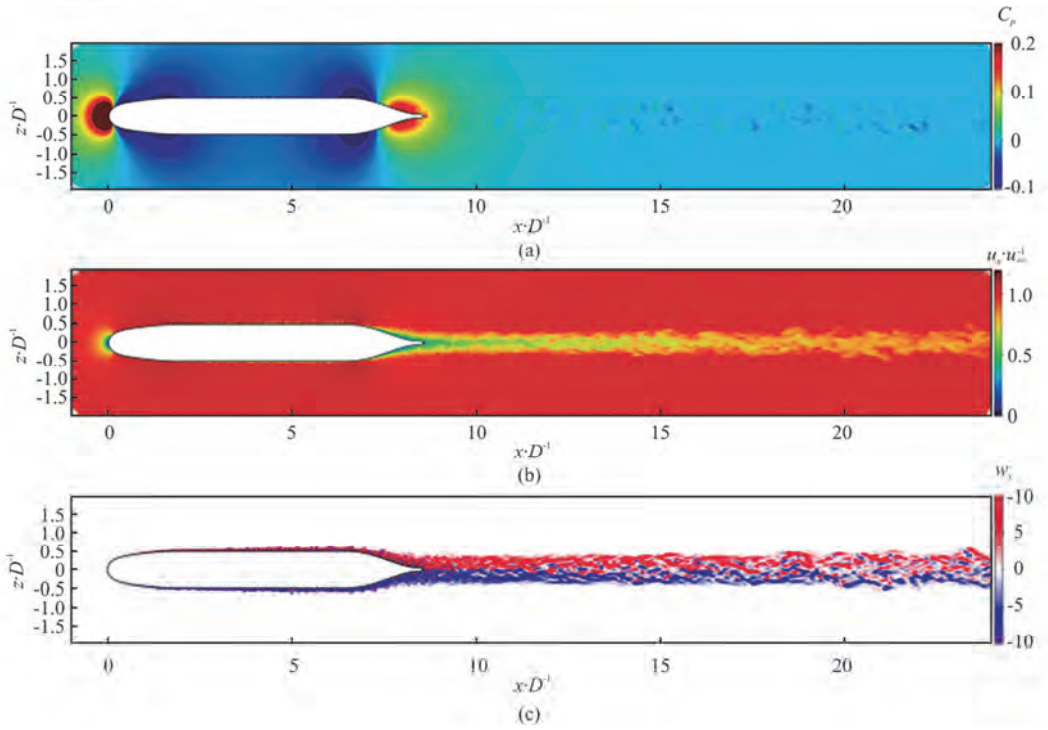

Fig. 5 (Color online) The instantaneous axial velocity normalized by u_∞, pressure coefficient C_p, and vorticity magnitude in xoz plane. The black solid lines represent the surface of hull

bow due to a favorable pressure gradient. Subsequently, it rapidly transitions to turbulence and develops downstream along the mid-body of the hull, characterized by a zero-pressure-gradient region. Typical wall-attached vortices in high Reynolds number[32-34] are observed on the mid-body as shown in Fig. 6. The axisymmetric TBL eventually undergoes separation at the stern, resulting in the formation of separation vortices and a wake, as illustrating in Fig. 7. The pressure gradient is insignificant in the wake area beyond the stern. Additionally, the gradual radial expansion of the wake is observable as it extends downstream along the hull.

3.2 *Time-averaged quantities*

Distributions of pressure and skin-friction coefficients on the hull are plotted in in Figs. 8, 9 together with the experimental results of Huang et al.[1] at

$Re_L = 1.2 \times 10^7$. The skin-friction coefficient is defined as

$$C_f = \frac{\tau_w}{0.5\rho u_\infty^2} \tag{7}$$

where τ_w is the magnitude of wall shear stress. Both pressure coefficient and skin-friction coefficient are in good agreement with experimental data.

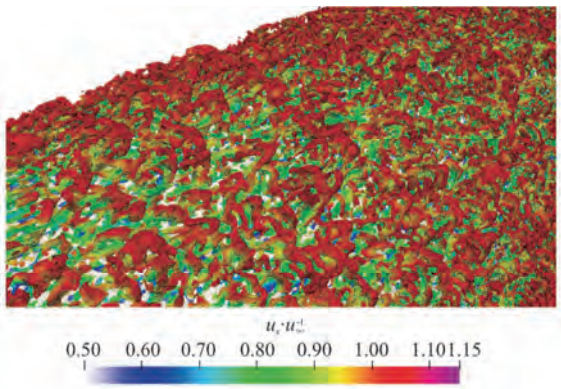

Fig. 6 (Color online) Typical wall attached vortices around the mid-body enlarged the region of mid-body from Fig. 4

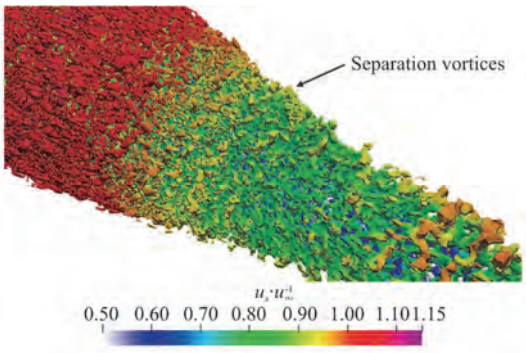

Fig. 7 (Color online) Separation vortices on the stern enlarged the region of stern from Fig. 4

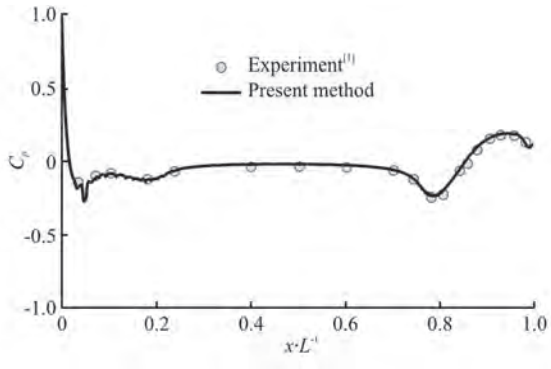

Fig. 8 Comparison of the distribution of time-averaged pressure coefficient with experimental results[1]

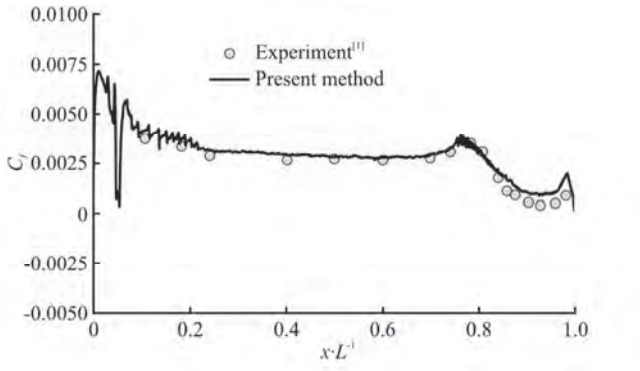

Fig. 9 Comparison of the distribution of time-averaged skin-friction coefficient with experimental results[1]

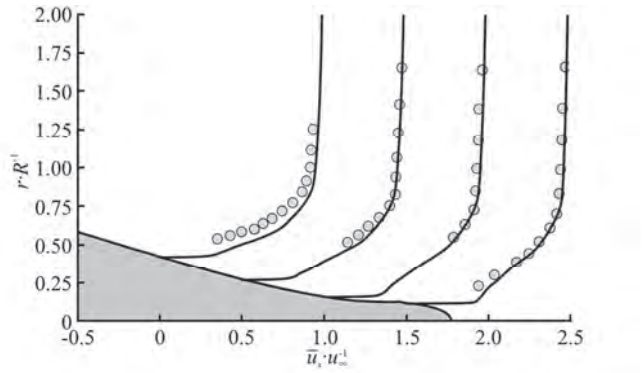

Fig. 10 Time-averaged axial velocity profiles at four streamwise locations, x / L = 0.904, 0.927, 0.956 and 0.978, on the stern are compared with experimental results[1]. The legend keeps the same with Fig. 8

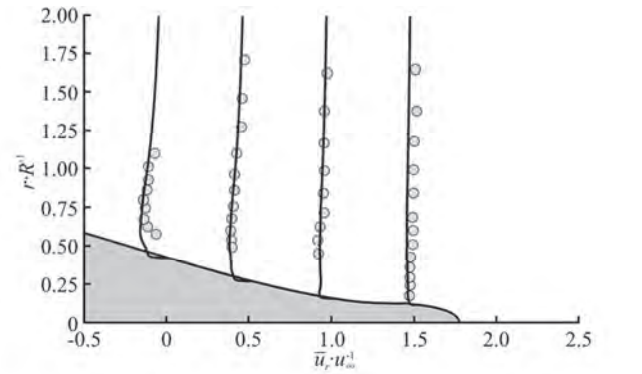

Fig. 11 Time-averaged radial velocity profiles at four streamwise locations, x / L = 0.904, 0.927, 0.956 and 0.978, on the stern are compared with experimental results[1]. The legend keeps the same with Fig. 8

Figures 10, 11 show profiles of time-averaged axial and radial velocity at four streamwise locations, x / L = 0.904, 0.927, 0.956 and 0.978, on the stern, together with experimental results of Huang et al.[1]. The evolution of the boundary layer at the stern is accurately replicated, leading to an increase in thickness due to the adverse pressure gradient[14]. The

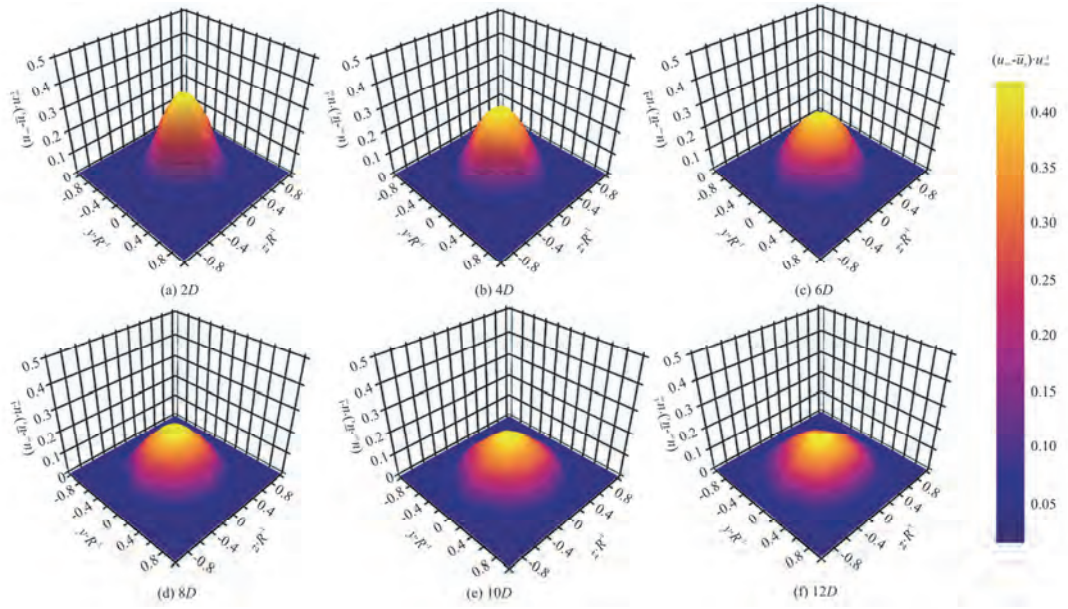

Fig. 12 (Color online) Distributions of time-averaged axial velocity defect in the wake of the hull in yoz plane. The six downstream locations are at increasing distances from the stern tail, with a step equal to twice of the maximum hull diameter, D

overall agreement between WMLES results and available experimental results is satisfactory except a minor overprediction in the velocity profile at $x/L = 0.904$.

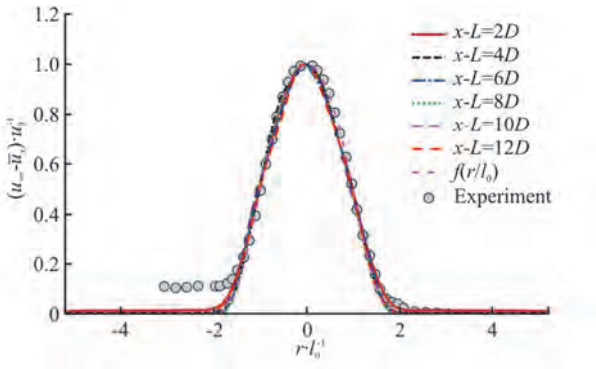

Fig. 13 (Color online) Time-averaged axial velocity defects in self-similar coordinates along the directions comparing with Eq. (8) and experimental results. Note that positive radial coordinates refer to the side upward

For the development of wake, distributions of time-averaged axial velocity defect in yoz plane are presented as shown in Fig. 12. Six downstream locations are at increasing distances from the stern up to 12 diameters downstream of the tail, with a step equal to twice of the maximum hull diameter. As the development of wake, the maximum velocity defect decreases gradually while the region of velocity defect increases which means the increase of wake width. Turbulent wake is usually characterized by the maximum velocity deficit, $u_0 = u_\infty - u_{CL}$ and half-wake width l_0, the distance between the centre of the wake and the position where the velocity deficit is equal to one half of u_0. u_{CL} is the velocity along the symmetry axis (center line) in wake. Then the distribution of time-averaged axial velocity defect in xoy plane in wake region can be expressed in a self-similar coordinate system by two scales u_0, l_0. The experimental data[3] at $Re_L = 1.2\times10^7$ and similarity law as Eq. (8) for the mean axial velocity proposed by Jiménez et al.[3] are also presented.

$$f(\eta) = \exp(-0.525\eta^2 - 0.1375\eta^4 - 0.03\eta^6 - 0.002225\eta^8) \quad (8)$$

where $\eta = r/l_0$.

The self-similarity of time-averaged axial velocity defect previously reported in the literature is clearly found and all profiles is very close, with a great agreement with experimental data and similarity law (Fig. 13). For the left side where $-4 < r/l_0 < -1.5$, the velocity defect in the numerical results is a little smaller than in the experiments due to the fact that this region is influenced by wake of fins[12].

3.3 *Turbulent fluctuation quantities*

Figure 14 provides a global view of the resolved turbulent kinematic energy (TKE), Reynold stress

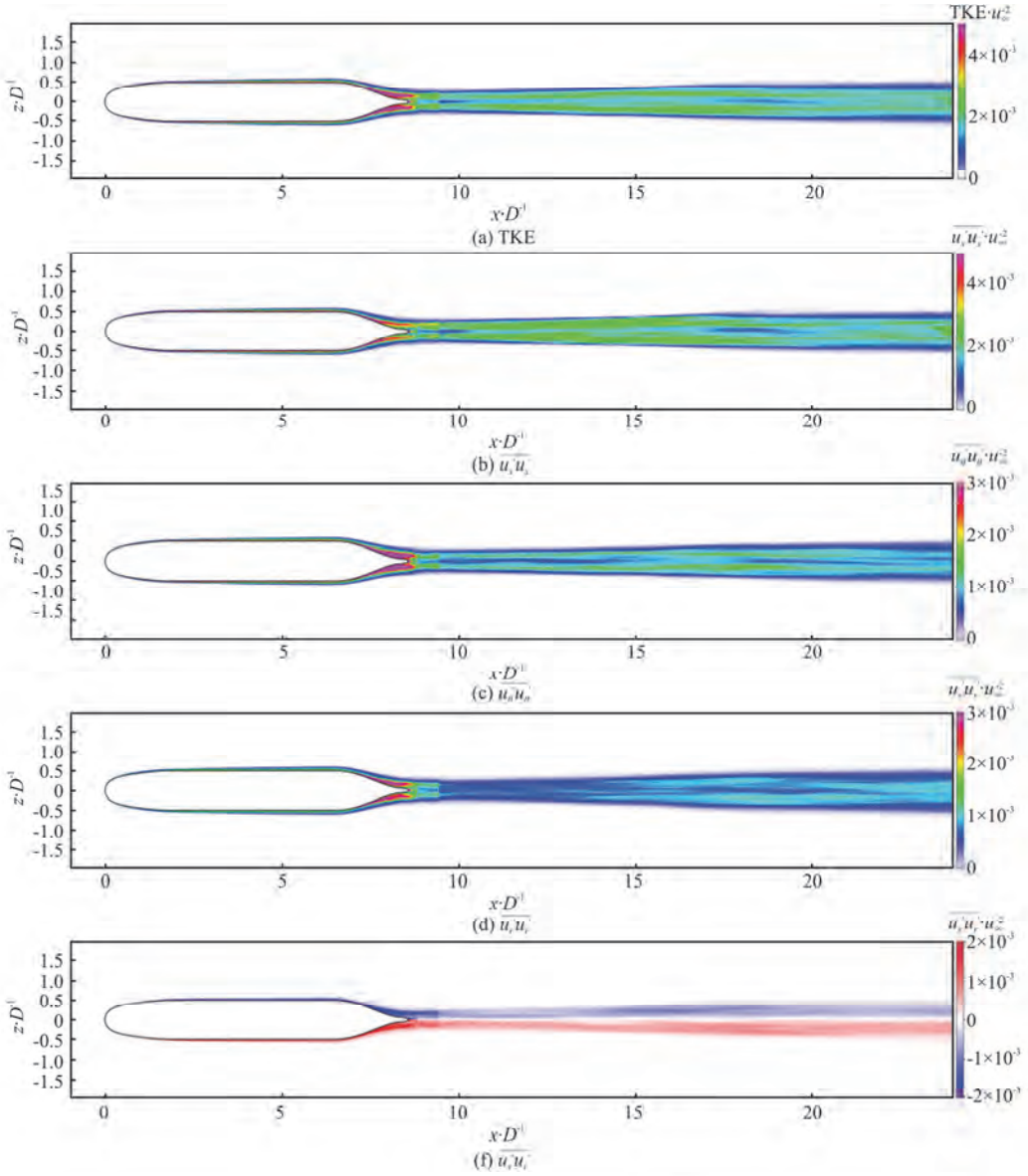

Fig. 14 (Color online) The second-order velocity statistics around the hull in xoz plane, normalized by u_∞^2

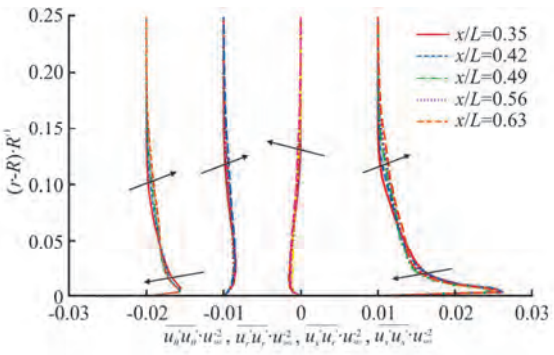

Fig. 15 (Color online) The streamwise growth of turbulent fluctuation quantities near the hull boundary layer at the mid-body. Arrows represent the direction of increasing x

$\overline{u_x'u_x'}$, $\overline{u_\theta'u_\theta'}$, $\overline{u_r'u_r'}$ and $\overline{u_x'u_r'}$ in yoz plane, normalized by u_∞^2, which are plotted with Turbulucid[31]. The wake of the hull is dominated by the axial turbulent intensity. For all second-order velocity statistics, the dual peak is clearly observed when turbulence flows over the stern and moves away from the hull. The profiles exhibit two symmetrical peaks away from the centerline in the yoz plane, consistent with the past work[11-12].

The streamwise growth of turbulent fluctuation quantities near the hull boundary layer at the mid-body is presented using profiles of Reynolds stress at multiple locations on the hull $(0.35 \le x/L \le 0.63)$ in Fig. 15. Minor difference is observed due to the minor pressure gradient at the mid-body.

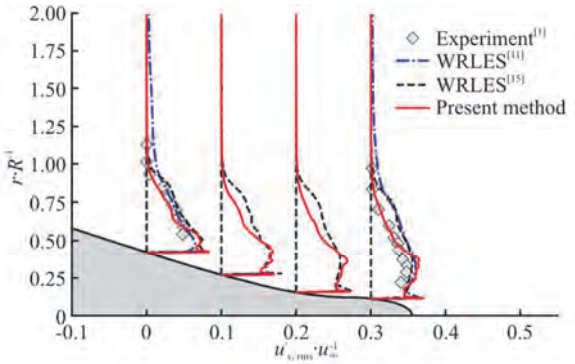

Fig. 16 (Color online) Profiles of rms of axial velocity at $x/L=$ 0.904, 0.927, 0.956 and 0.978. Diamonds show the experimental results by Huang et al.[1] at $Re_L=1.2\times10^7$. The LES results at $Re_L=1.2\times10^6$ presented by Kumar and Mahesh[11], Liu et al.[15] are also shown for comparison

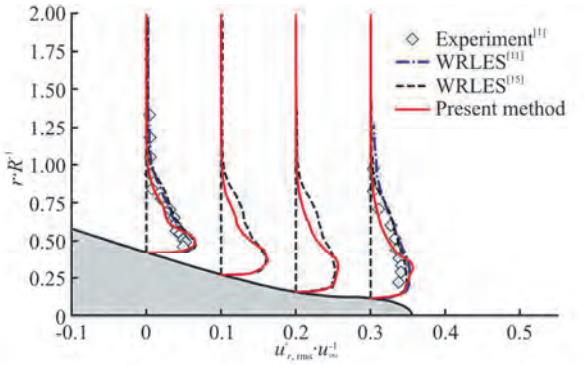

Fig. 17 (Color online) Profiles of rms of radial velocity at $x/L=$ 0.904, 0.927, 0.956, and 0.978. Diamonds show the experimental results by Huang et al.[1] at $Re_L=1.2\times10^7$. The WRLES results at $Re_L=1.2\times10^6$ presented by Kumar and Mahesh[11], Liu et al.[15] are also shown for comparison

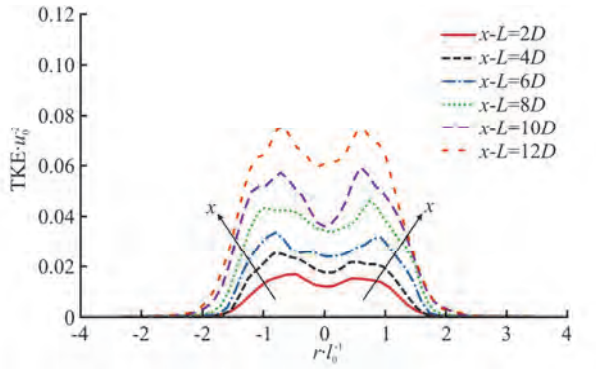

Fig. 18 (Color online) Profiles of TKE normalized by u_0^2 at six streamwise locations, $x-L=2D$, $4D$, $6D$, $8D$, $10D$ and $12D$ in xoz plane in the wake. Note that positive radial coordinates refer to the side upward

In order to further analyze the reliability of the simulation to capture turbulent fluctuation quantities, profiles of rms of axial and radial velocity at $x/L=$ 0.904, 0.927, 0.956 and 0.978 are shown in Figs. 16, 17. Experimental results by Huang et al.[1] at $Re_L=1.2\times10^7$ and WRLES results at $Re_L=1.2\times10^6$ presented by Kumar and Mahesh[11], Liu et al.[15] are also shown for comparison. It is remarkable that present WMLES results show a good agreement about axial velocity fluctuations with experimental data and WRLES results. Furthermore, the agreement is satisfactory even when dealing with fluctuations in radial velocity, a task known for its complexity in capturing[15].

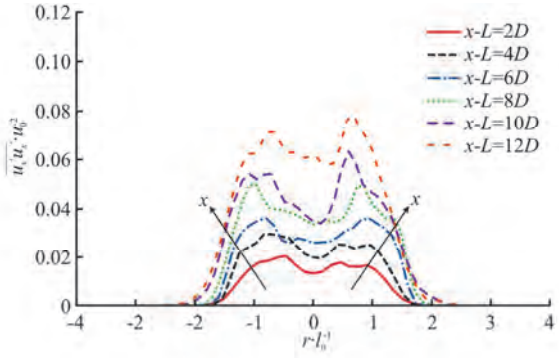

Fig. 19 (Color online) Profiles of $\overline{u'_x u'_x}$ normalized by u_0^2 at six streamwise locations, $x-L=2D$, $4D$, $6D$, $8D$, $10D$ and $12D$ in xoz plane in the wake. Note that positive radial coordinates refer to the side upward

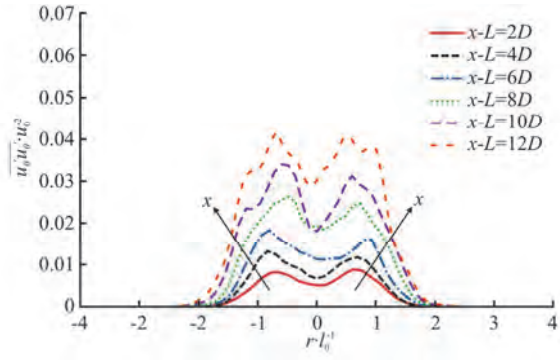

Fig. 20 (Color online) Profiles of $\overline{u'_\theta u'_\theta}$ normalized by u_0^2 at six streamwise locations, $x-L=2D$, $4D$, $6D$, $8D$, $10D$ and $12D$ in xoz plane in the wake. Note that positive radial coordinates refer to the side Upward

For the turbulent fluctuation quantities in wake, distributions of resolved TKE and Reynold stress are investigated at six streamwise locations, $x-L=2D$, $4D$, $6D$, $8D$, $10D$ and $12D$ in xoz plane in

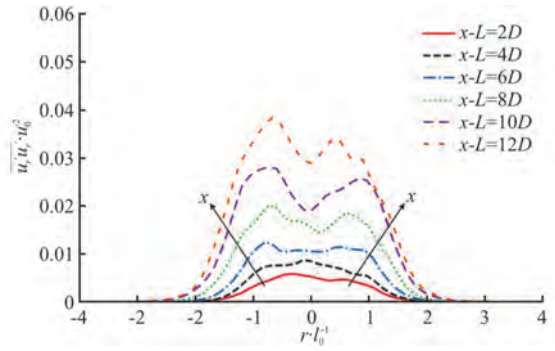

Fig. 21 (Color online) Profiles of $\overline{u_r'u_r'}$ normalized by u_0^2 at six streamwise locations, $x-L=2D$, $4D$, $6D$, $8D$, $10D$ and $12D$ in xoz plane in the wake. Note that positive radial coordinates refer to the side upward

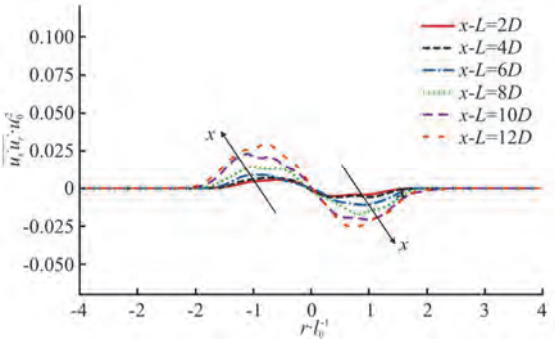

Fig. 22 (Color online) Profiles of $\overline{u_x'u_r'}$ normalized by u_0^2 at six streamwise locations, $x-L=2D$, $4D$, $6D$, $8D$, $10D$ and $12D$ in xoz plane in the wake. Note that positive radial coordinates refer to the side upward

the wake. All profiles are expressed in the self-similar coordinate system as shown in Figs. 18-22. Turbulent fluctuation quantities are normalized by u_0^2. The dual peak feature is obvious observed again as the development of wake. Otherwise, all of turbulent fluctuation quantities show non-self-similar. The decay in turbulent fluctuation quantities occurs at a slower rate than that of momentum deficit, which implies a rise in self-similar coordinates as the development of wake.

4. Conclusions

In this study, turbulent fluctuations around an axisymmetric body of revolution (DARPA SUBOFF bare model) are numerically investigated at $Re_L = 1.2\times10^7$ with WMLES. The objective is to evaluate the ability of WMLES to predict turbulent fluctuations over the axisymmetric hull and to investigate the evolution of fluctuation quantities of the flow field around the body of the DARPA SUBOFF.

Instantaneous near-wall flow structures are accurately identified using the modified normalized Liutex-Omega method. Key flow features about the TBL development over the surface of SUBOFF and its wake are effectively captured.

Time-averaged flow quantities, including pressure coefficient, skin-friction coefficient, and stern velocity profiles, have been meticulously validated, showing excellent agreements with experimental data. The self-similarity of the velocity defect is found when expressed within self-similar coordinates, extending up to twelve diameters from the tail. Furthermore, a satisfactory agreement with available experimental data and empirical equation is achieved.

A comprehensive investigation is conducted on second-order statistics of the mid-body, stern, and wake regions. The present numerical method is found to provide a good quantitative agreement on rms of radial and axial fluctuating velocities on the stern with experimental data and previous WRLES results. The decay in turbulent fluctuation quantities is observed at a slower rate than that of momentum deficit, which shows a rise in self-similar coordinates over the development of wake. The dual peak feature is obviously observed. TKE and other second-order statistics of velocity are found not self-similar over the length of the wake.

In the future, wall-pressure fluctuations will be further investigated with WMLES. Different wall stress modeling strategies will be also studied and developed to improve the accuracy of WMLES.

Acknowledgement

(This research received other funding agency in the public, commercial, or not-for-profit sectors.)

Compliance with ethical standards

Conflict of interest: The authors declare that they have no conflict of interest. Wei-wen Zhao, Jian-hua Wang and De-cheng Wan are editorial board members for the Journal of Hydrodynamics and was not involved in the editorial review, or the decision to publish this article. All authors declare that there are no other competing interests.

Ethical approval: This article does not contain any studies with human participants or animals performed by any of the authors.

Informed consent: Informed consent was obtained from all individual participants included in the study.

References

[1] Huang T., Liu H., Groves N. et al. Measurements of flows

over an axisymmetric body with various appendages in a wind tunnel: The DARPA SUBOFF experimental program [C]. *Proceedings of the 19th Symposium on Naval Hydrodynamics*, Seoul, Korea, 1992.
[2] Jiménez J., Reynolds R., Smits A. The effects of fins on the intermediate wake of a submarine model [J]. *Journal of Fluids Engineering*, 2010, 132(3): 031102.
[3] Jiménez J. M., Hultmark M., Smits A. J. The intermediate wake of a body of revolution at high Reynolds numbers [J]. *Journal of Fluid Mechanics*, 2010, 659: 516-539.
[4] Boger D., Dreyer J. Prediction of hydrodynamic forces and moments for underwater vehicles using overset grids [C]. *The 44th AIAA Aerospace Sciences Meeting and Exhibit*, Reno, USA, 2006.
[5] Cao L., Zhu J., Zeng G. Viscous-flow calculations of submarine maneuvering hydrodynamic coefficients and flow field based on same grid topology [J]. *Journal of Applied Fluid Mechanics*, 2016. 9(2): 817-826.
[6] Manshadi M., Hejranfar K., Farajollahi A. Effect of vortex generators on hydrodynamic behavior of an underwater axisymmetric hull at high angles of attack [J]. *Journal of Visualization*, 2017, 20(3): 559-579.
[7] Gao T., Wang Y., Pang Y. et al. A time-efficient CFD approach for hydrodynamic coefficient determination and model simplification of submarine [J]. *Ocean Engineering*, 2018, 154: 16-26.
[8] Wang Y., Gao T., Pang Y. et al. Investigation and optimization of appendage influence on the hydrodynamic performance of AUVs [J]. *Journal of Marine Science and Technology*, 2019, 24(1): 297-305.
[9] Alin N., Bensow R., Fureby C. et al. Current capabilities of DES and LES for submarines at straight course [J]. *Journal of Ship Research*, 2010, 54(3): 184-196.
[10] Zhao W. W., Zhou F., Fan G. et al. Assessment of subgrid-scale models in wall-modeled large-eddy simulations of turbulent channel flows [J]. *Journal of Hydrodynamics*, 2023, 35(3): 407-416.
[11] Kumar P., Mahesh K. Large-eddy simulation of flow over an axisymmetric body of revolution [J]. *Journal of Fluid Mechanics*, 2018, 853: 537-563.
[12] Posa A., Balaras E. A numerical investigation of the wake of an axisymmetric body with appendages [J]. *Journal of Fluid Mechanics*, 2016, 792: 470-498.
[13] Posa A., Balaras E. A numerical investigation about the effects of Reynolds number on the flow around an appended axisymmetric body of revolution [J]. *Journal of Fluid Mechanics*, 2020, 884: A41.
[14] Morse N., Mahesh K. Large-eddy simulation and streamline coordinate analysis of flow over an axisymmetric hull [J]. *Journal of Fluid Mechanics*, 2021, 926: A18.
[15] Liu Y., Wang H., Wang S. et al. A cache-efficient reordering method for unstructured meshes with applications to wall-resolved large-eddy simulations [J]. *Journal of Computational Physics*, 2023, 480: 112009.
[16] Coulier A. Multiscale modeling in systems biology: Methods and perspectives [D]. Uppsala, Sweden: Uppsala University, 2021.
[17] Choi H., Moin P. Grid-point requirements for large eddy simulation: Chapman's estimates revisited [J]. *Physics of Fluids*, 2012, 24(1): 011702.
[18] Larsson J., Kawai S., Bodart J. et al. Large eddy simulation with modeled wall-stress: recent progress and future directions [J]. *Mechanical Engineering Reviews*, 2016, 3(1): 1-23.
[19] Georgiadis N., Rizzetta D., Fureby C. Large-eddy simulation: Current capabilities, recommended practices, and future research [J]. *AIAA Journal*, 2010, 48(8): 1772-1784.
[20] Bose S. T., Park G. I. Wall-modeled large-eddy simulation for complex turbulent flows [J]. *Annual Review of Fluid Mechanics*, 2018, 50(1): 535-561.
[21] Zhou D., Wang K., Wang M. Large-eddy simulation of an axisymmetric boundary layer on a body of revolution [C]. *Proceeding of AIAA Aviation Forum*, 2022.
[22] Zhou Z. T., Xu Z. Y., Wang S. Z. et al. Wall-modeled large-eddy simulation of noise generated by turbulence around an appended axisymmetric body of revolution [J]. *Journal of Hydrodynamics*, 2022, 34(4): 533-554.
[23] Chen S. T., Yang L. C., Zhao W. W. et al. Wall-modeled large eddy simulation for the flows around an axisymmetric body of revolution [J]. *Journal of Hydrodynamics*, 2023, 35(2): 199-209.
[24] Mukha T., Rezaeiravesh S., Liefvendahl M. A library for wall-modelled large-eddy simulation based on OpenFOAM technology [J]. *Computer Physics Communications*, 2019, 239: 204-224.
[25] Nicoud F., Ducros F. Subgrid-scale stress modelling based on the square of the velocity gradient tensor [J]. *Flow, Turbulence and Combustion*, 1999, 62(3): 183-200.
[26] Cabot W., Moin P. Approximate wall boundary conditions in the large-eddy simulation of high Reynolds number flow. Flow [J], *Turbulence and Combustion*, 2000, 63: 269-291.
[27] Menter F. R. Two-equation eddy-viscosity turbulence models for engineering applications [J]. *AIAA Journal*, 1994, 32(8): 1598-1605.
[28] Liu C., Yu Y. Mathematical foundation of Liutex theory [J]. *Journal of Hydrodynamics*, 2022, 34(6): 981-993.
[29] Pang B. Y., Yu Z. D., Yan B. W. et al. Identification of vortex boundaries in two-dimensional incompressible flows based on the Liutex-shear interaction [J]. *Journal of Hydrodynamics,* 2023, 35(5): 825-831.
[30] Zhao W. W., Wang J. H., Wan D. C. Vortex identification methods in marine hydrodynamics [J]. *Journal of Hydrodynamics*, 2020, 32(2): 286-295.
[31] Mukha T. Turbulucid: A Python package for post-processing of fluid flow simulations [J]. *Journal of Open Research Software*, 2018, 6(1): 23.
[32] Smits A., McKeon B., Marusic I. High–Reynolds number wall turbulence [J]. *Annual Review of Fluid Mechanics*, 2011, 43(1): 353-375.
[33] Wang L., Pan C., Wang J. et al. Statistical signatures of component wall-attached eddies in proper orthogonal decomposition modes of a turbulent boundary layer [J]. *Journal of Fluid Mechanics*, 2022, 944: A26.
[34] Wang L., Pan C., Wang J. Wall-attached and wall-detached eddies in proper orthogonal decomposition modes of a turbulent channel flow [J]. *Physics of Fluids*, 2022, 34(9): 095124.